A Nonhydrostatic Mesoscale Ocean Model. Part II: Numerical Implementation

AMALA MAHADEVAN

Department of Geophysical Sciences, University of Chicago, Chicago, Illinois

JOSEPH OLIGER

Department of Computer Science, Stanford University, Stanford, California

ROBERT STREET

Environmental Fluid Mechanics Laboratory, Stanford University, Stanford, California

(Manuscript received 13 March 1995, in final form 27 February 1996)

ABSTRACT

The nonhydrostatic model with a free surface is numerically implemented in boundary-fitted curvilinear coordinates to model the mesoscale circulation in an ocean basin with natural topography. A semi-implicit numerical scheme is used, and the directional inhomogeneity in the elliptic equation for pressure is exploited to speed up the computation of its solution while using the multigrid method.

The model is used to simulate the circulation in the Gulf of Mexico. We observe the formation of the Loop Current and several eddies. The flow is very strongly controlled by the topography and our numerical experiments reveal that in the bottom layers, the flow along topographic contours is in the opposite direction of the anticyclonic circulation in the top layers.

1. Introduction

Much of the ocean's kinetic energy is manifest in (10–100-km length) *meso*scale motions, as in meandering currents and eddies. Such motions play a significant role in the ocean's climate and in transporting heat, salt, and momentum. The associated flow fields are three-dimensional, time dependent, and characterized by horizontal velocities of $0.1-1\ \mathrm{m\ s^{-1}}$, a small ratio of depth to length scales, and Rossby numbers in the range $10^{-1}-10^{-2}$. Our interest lies in modeling such motions in a region of the ocean.

In the preceding paper, Mahadevan et al. (1996), we developed an accurate three-dimensional model for mesoscale flow that is well-posed in domains with open or solid boundaries. The model is "quasi"-nonhydrostatic, in that it permits a greater deviation from hydrostatic balance than exists in the ocean. This approximation is used instead of the usual hydrostatic approximation to alleviate the demand on the high accuracy that is needed (but difficult to maintain) in integrating the vertical momentum equation. Unlike the hydrostatic (*primitive*) equations, this model is accurate in all three-dimensions and is well-posed in domains with open boundaries. These attributes are of importance in mesoscale modeling where modeling the small but relevant vertical velocity is important, and open boundaries are inevitable. Mesoscale features are often localized and the resolution required for them is presently unaffordable for the entire world's oceans. The model has a free surface. The boundary condition at the top surface is thus accurate and does not corrupt the vertical velocity field as does the rigid-lid approximation.

In this work, we develop an efficient numerical solution procedure for the model and put it to test in the Gulf of Mexico. We numerically integrate the equation for the free-surface position and terms involving the free-surface pressure gradient implicitly, while treating the other terms explicitly. Thus, the gravity wave speed, which is 10^2-10^3 times that of the fluid, does not govern the time step of integration. We use a multistage time integration scheme, and both the implicit and explicit parts share the same time stages. The free-surface position itself is computed by solving a two-dimensional elliptic equation.

Being nonhydrostatic, the model requires that we compute the three-dimensional pressure field using an iterative procedure. This is computationally intensive, and is what often deters modelers from using the nonhydrostatic equations unless nonhydrostatic effects are significant as in open ocean convection (Jones and

Corresponding author address: Dr. Amala Mahadevan, Department of Geophysical Sciences, University of Chicago, 5734 S. Ellis Street, Chicago, IL 60637.
E-mail: amala@popeye.uchicago.edu

Marshall 1993). In the free-surface formulation of the model used here, we take advantage of the inhomogeneity (that results from near hydrostatic balance) in the elliptic equation for the nonhydrostatic component of pressure, to speed up the solution procedure by a factor of 5–8 over the corresponding rigid-lid problem. The solution of these equations is viable even on a workstation and is only a few times more expensive than that of the hydrostatic equations.

The numerical model is developed with the following features.

1) It can be used in a domain with a complex geometry such as that of a natural ocean basin. A curvilinear body-fitted grid is used to discretize the ocean basin with its undulating bottom topography, curved lateral boundaries, and free surface.

2) The model is well-posed. It may have solid or open lateral boundaries, provided the necessary boundary condition data is available at these.

3) The top boundary of the domain is a free surface. The grid reconfigures itself to this boundary as it moves in time. A semi-implicit discretization of the free surface overcomes the restriction on the time step imposed by the speed of the external gravity waves.

4) A finite volume formulation is used and the equation of continuity is satisfied in the discrete sense. Scalar variables are also conserved. The "QUICK" scheme (Leonard 1979) is used for the advective terms.

5) A multigrid solver is written to speed up the solution of the three-dimensional elliptic equation for the nonhydrostatic pressure field. The decoupling of the pressure into hydrostatic and nonhydrostatic components enables taking advantage of the shallowness of the flow and makes the computation of the three-dimensional nonhydrostatic pressure field extremely fast.

6) The numerical procedure is made efficient so that we can integrate the equations over sufficiently long periods of time to observe the development of the mesoscale flow.

7) The model does not rely on an eddy viscosity term for its stability. This is important since viscous effects are negligibly small at the length scales that are of interest to us.

We use the model to simulate the mesoscale circulations in the Gulf of Mexico driven by the inflow and outflow. The effects of wind forcing, as well as heat and salt fluxes are thought to be less dominant than the inflow and outflow forcing and are neglected from the model for the present. Observations made under different conditions give us some insight into the physics of such flows, and into the effect of various factors on the circulation. We find the circulation in the gulf to be very strongly driven by the topography.

In what follows, we begin by presenting the equations that comprise the model in section 2. In sections 3–5 we describe the numerical implementation of the model in curvilinear coordinates and explain the speedup we are able to achieve in solving the elliptic equation for pressure. In sections 6–8 we apply the model to simulating the mesoscale circulation in the Gulf of Mexico and present some analysis to explain our numerical results.

2. The model equations

Neglecting viscous effects, diffusion of heat and salt, wind forcing, and fluxes of heat and salt, the dimensionless equations that constitute the quasi-nonhydrostatic free-surface model for mesoscale flow are

$$\frac{Ds}{Dt} = 0 \tag{2.1a}$$

$$\frac{DT}{Dt} = 0 \tag{2.1b}$$

$$\frac{Du}{Dt} + \frac{1}{\epsilon}(gh_x + r_x + \delta q_x - fv + \epsilon\delta bw) = 0 \tag{2.1c}$$

$$\frac{Dv}{Dt} + \frac{1}{\epsilon}(gh_y + r_y + \delta q_y + fu) = 0 \tag{2.1d}$$

$$\frac{Dw}{Dt} + \beta\left(q_z - bu - \epsilon\lambda\frac{(u^2 + v^2)}{a}\right) = 0 \tag{2.1e}$$

$$u_x + v_y + \epsilon w_z = 0 \tag{2.1f}$$

$$\rho = \rho(s, T) \tag{2.1g}$$

$$\frac{\partial h}{\partial t} + \frac{\epsilon}{\mathcal{F}^2}\left[\frac{\partial}{\partial x}\left(\int_{-d}^{H/Dh} u\,dz\right) + \frac{\partial}{\partial y}\left(\int_{-d}^{H/Dh} v\,dz\right)\right] = 0, \tag{2.1h}$$

where

$$\frac{D}{Dt} \equiv u\frac{\partial}{\partial x} + v\frac{\partial}{\partial y} + \epsilon w\frac{\partial}{\partial z}.$$

Here x and y are defined as eastward and northward distances along the surface of the globe, z is the distance from the surface of the globe in a direction antiparallel to gravity, and t is time. The dimensionless Coriolis parameters f and b are twice the earth's angular velocity resolved normal and tangential to the earth's surface at a given point. The velocity components u, v, w are in the x, y, z directions, respectively. The variable s represents the salinity, T the potential temperature, h the elevation of the free surface, q the nonhydrostatic component of the pressure, r the hydrostatic pressure due to density variations from the mean, ρ the potential density, and a the distance from the center of the earth. All the quantities have been nondimensionalized so that they and their derivatives are order 1. The dimensionless parameter λ is the ratio of the characteristic horizontal length scale to a characteristic value of the earth's radius, δ is the aspect ratio

or ratio of depth to length scales, ϵ is the Rossby number, $\mathcal{F}$ is the Froude number, and H/D is the ratio of characteristic free-surface elevation to depth scale.

Equation (2.1g) is an equation of state for potential density. In these equations we resort to the Boussinesq approximation. Forcing terms, and any parameterization for subgrid-scale motions may be added. The dimensionless coefficient that would appear in the exact vertical momentum equation is replaced by a relaxation parameter β that is much smaller than it. The relative solution error due to this relaxation is $O(\beta^{-1})$. The scaling of the equations and development of the model is described in detail in Mahadevan et al. (1996).

3. Numerical framework

a. The boundary fitted curvilinear coordinate system

In order to model the natural geometry of a region of the ocean, we discretize our ocean domain with a smooth boundary fitted curvilinear grid that maps into a uniformly discretized cube in which we solve the equations. The mapping from the computational to physical space, where the variables are ξ_i and x_i, respectively, is defined in terms of the transformation Jacobian $d_{xy} \equiv \partial x_i / \partial \xi_j$ or its inverse. Only the independent variables (t, x, y, z) in the physical space are transformed into $(\tau, \xi, \eta, \sigma)$ in the computational space, with the dependent variables retaining their Cartesian orientations. Such coordinate transformations are described in many places in the literature, for example, in Meakin and Street (1988), Perng (1990), and Zang et al. (1994).

The ocean surface of the region we are modeling is mapped onto the top face of the cube in our computational domain. The bottom face corresponds to the ocean bottom. The lateral faces are the four lateral boundaries of the region and are taken to be vertical surfaces. When the lateral boundary is a coastline, we approximate it by a vertical wall of certain minimum height that maintains the required minimum grid spacing for numerical stability.

In the vertical, we use a σ-coordinate system that configures smoothly to the undulating bottom topography and to the free surface. We define it as

$$\sigma = \left(\frac{z + d}{h + d}\right) \cdot N_k, \tag{3.1}$$

where N_k is the number of grid intervals in the vertical direction, d is the depth of the ocean floor, h is the free-surface elevation, and z is measured positive upward with reference to the mean sea level. The grid interval $\Delta\sigma$ is taken to be 1. Equation (3.1) is differentiated to obtain σ_t, σ_x, σ_y, σ_z, and could easily be modified for a stretched grid or a grid in which only the top few layers reconfigure to the changing free surface.

In plan view, we discretize the domain by a smooth curvilinear grid in (ξ, η) that remains fixed in time. When viewed from the top, this grid is the same at each of the σ levels. Hence

$$\xi_t = 0, \quad \eta_t = 0, \quad \xi_z = 0, \quad \eta_z = 0.$$

Since the time variable is unchanged by the mapping, that is, $\tau = t$, it is independent of the spatial coordinates and

$$\tau_t = 1, \quad \tau_x = 0, \quad \tau_y = 0, \quad \tau_z = 0.$$

Usually x_ξ, x_η, y_ξ, x_η are available from the grid generation, but we can easily convert them to ξ_x, ξ_y, η_x, η_y using

$$d_{\xi\eta} \equiv \frac{\partial \xi_i}{\partial x_j} = d_{xy}^{-1} = \begin{pmatrix} 1 & 0 & 0 & 0 \\ 0 & y_\eta/J_{2d} & -x_\eta/J_{2d} & 0 \\ 0 & -y_\xi/J_{2d} & x_\xi/J_{2d} & 0 \\ -z_\tau/z_\sigma & (y_\xi z_\eta - y_\eta z_\xi)/J_{2d} & (x_\eta z_\xi - x_\xi z_\eta)/J_{2d} & 1/z_\sigma \end{pmatrix}, \tag{3.2}$$

where $J \equiv \det(d_{xy})$ and $J_{2d} \equiv x_\xi y_\eta - x_\eta y_\xi = \sigma_z J$.

b. The equations in strong conservation law form and their transformation to curvilinear coordinates

We convert the equations into strong conservation law form before solving them numerically. Using the continuity equation (2.1f), we rewrite the dimensionless time-dependent equations (2.1) as

$$\frac{\partial}{\partial t}\begin{pmatrix} s \\ T \\ u \\ v \\ w \end{pmatrix} + \frac{\partial}{\partial x}\begin{pmatrix} us \\ uT \\ u^2 + p/\epsilon \\ uv \\ uw \end{pmatrix} + \frac{\partial}{\partial y}\begin{pmatrix} vs \\ vT \\ uv \\ v^2 + p/\epsilon \\ vw \end{pmatrix} + \frac{\partial}{\partial z}\begin{pmatrix} \epsilon ws \\ \epsilon wT \\ \epsilon uw \\ \epsilon vw \\ \epsilon w^2 + \beta q \end{pmatrix} + \begin{pmatrix} 0 \\ 0 \\ -fv/\epsilon + \delta bw \\ fu/\epsilon \\ -\beta bu \end{pmatrix} = 0, \tag{3.3}$$

where

$$p \equiv gh + r + \delta q.$$

We have neglected the curvature term $-\beta\epsilon\lambda(u^2 + v^2)a^{-1}$ since we will be using a value of $\beta \ll (\epsilon\lambda)^{-1}$.

The system of equations (3.3) can be written as

$$\frac{\partial \mathbf{F}_j}{\partial x_j} + \mathbf{S} = 0,$$

where x_j are the components of (t, x, y, z) and $\mathbf{F}_j$ and $\mathbf{S}$ are the corresponding vectors in (3.3). Applying the chain rule to this system, multiplying through by $J \equiv \det(\partial x_i/\partial \xi_j)$ and using the metric identity

$$\frac{\partial}{\partial \xi_m}\left(J\frac{\partial \xi_m}{\partial x_i}\right) = 0, \tag{3.4}$$

we get

$$\frac{\partial}{\partial t}\begin{pmatrix} Js \\ JT \\ Ju \\ Jv \\ Jw \end{pmatrix} + \frac{\partial}{\partial \xi}\begin{pmatrix} Us \\ UT \\ Uu \\ Uv \\ Uw \end{pmatrix} + \frac{\partial}{\partial \eta}\begin{pmatrix} Vs \\ VT \\ Vu \\ Vv \\ Vw \end{pmatrix} + \frac{\partial}{\partial \sigma}\begin{pmatrix} Ws \\ WT \\ Wu \\ Wv \\ Ww \end{pmatrix} + \begin{pmatrix} 0 \\ 0 \\ J(p_\xi \xi_x + p_\eta \eta_x + p_\sigma \sigma_x - fv + \epsilon\delta bw)/\epsilon \\ J(p_\xi \xi_y + p_\eta \eta_y + p_\sigma \sigma_y + fu)/\epsilon \\ J\beta(q_\sigma \sigma_z - bu) \end{pmatrix} = 0, \tag{3.5}$$

where

$$U \equiv J(u\xi_x + v\xi_y)$$

$$V \equiv J(u\eta_x + v\eta_y)$$

$$W \equiv J(\sigma_t + u\sigma_x + v\sigma_y + \epsilon w\sigma_z) \tag{3.6}$$

represent the volume fluxes across the cell faces per unit time. They are equal to the contravariant velocity components multiplied by the area of the cell face to which they are normal. The relation between u, v, w and U, V, W is expressed by

$$\mathbf{U} = Jd_{\xi\eta}\mathbf{u}, \tag{3.7}$$

where

$$\mathbf{U} \equiv (J, U, V, W)^{-1} \quad \mathbf{u} = (1, u, v, \epsilon w)^{-1} \tag{3.8}$$

and $d_{\xi\eta}$ is defined in (3.2). The parameter ϵ enters the definition of W due to the scaling (because the quantities x, y, z, u, v, w, etc. are all dimensionless quantities). The definition of W takes into account the movement of the grid in the σ direction.

Similarly, using the chain rule and metric identity (3.4), we transform the continuity equation (2.1f) into

$$\frac{\partial J}{\partial \tau} + \frac{\partial U}{\partial \xi} + \frac{\partial V}{\partial \eta} + \frac{\partial W}{\partial \sigma} = 0. \tag{3.9}$$

The quantity $\partial J/\partial \tau$ represents the change in volume of a grid cell per unit time. A more convenient form of the continuity equation is

$$\frac{\partial U}{\partial \xi} + \frac{\partial V}{\partial \eta} + \frac{\partial \mathcal{W}}{\partial \sigma} = 0, \tag{3.10}$$

where

$$\mathcal{W} \equiv J(u\sigma_x + v\sigma_y + \epsilon w\sigma_z) \tag{3.11}$$

and differs from W by $J\sigma_t$.

Equation (2.1h) for the free surface is mapped from (t, x, y) space to (τ, ξ, η) space using the two-dimensional (2D) transformation matrix

$$d_{xy}^{2d} \equiv \begin{pmatrix} t_\tau & t_\xi & t_\eta \\ x_\tau & x_\xi & x_\eta \\ y_\tau & y_\xi & y_\eta \end{pmatrix} = \begin{pmatrix} 1 & 0 & 0 \\ 0 & x_\xi & x_\eta \\ 0 & y_\xi & y_\eta \end{pmatrix}.$$

The 2D Jacobian $J_{2d} \equiv \det(d_{xy}^{2d}) = x_\xi y_\eta - x_\eta y_\xi$ represents the area of the top face of a grid cell. Expressing (2.1h) in the form

$$\frac{H}{D}\frac{\partial h}{\partial t} + \left(\frac{\partial F_i}{\partial x_i}\right)_{i=1,2} = 0,$$

where x_i corresponds to x, y and $\mathcal{F}^2/\epsilon = H/D$, multiplying by J_{2d}, using the chain rule and the metric identity in 2D, gives the following equation for the free surface in flux variables:

$$J_{2d}\frac{H}{D}\frac{\partial h}{\partial \tau} + \frac{\partial}{\partial \xi}\left(\int_0^{N_k} U d\sigma\right) + \frac{\partial}{\partial \eta}\left(\int_0^{N_k} V d\sigma\right) = 0. \tag{3.12}$$

c. *Boundary conditions in the transformed coordinates*

The boundary conditions that we specify in our problem are the flux quantities U^{n+1} at ξ = const lateral boundaries, V^{n+1} at η = const lateral boundaries, W^{n+1} at the bottom boundary $\sigma = 0$, and the pressure at the free surface. The flux across a solid boundary is zero. At an open boundary (inflow or outflow), we prescribe the flux cellwise across the boundary surface. We have the option of prescribing the pressure instead of the cellwise flux at the outflow. Since the flux is the normal velocity multiplied by the surface area, specifying the flux is equivalent to specifying the normal velocity and surface area at a boundary. At the inflow we must spec-

ify s, T and the complete velocity vector, which includes the normal and tangential velocity components.

d. Arrangement of the grid and variables

We use a control volume formulation and position the variables as in Zang et al. (1994). The variables p, q, r, s, T, u, v, w are specified at centers of the computational cells. The grid indices i, j, k correspond to the ξ, η, σ directions. The number of grid intervals in each direction is denoted by N_i, N_j, N_k. Since $\Delta\xi = \Delta\eta = \Delta\sigma = 1$, the values of ξ, η, σ coincide with the grid indices i, j, k and range from 0 at one boundary surface to N_i, N_j or N_k at the opposite boundary surface of the domain. The grid cells are referenced by i, j, k, where $i = 1, \cdots, N_i, j = 1, \cdots, N_j, k = 1, \cdots, N_k$ inside the domain. In addition to the interior cells, there is a single layer of "ghost" cells outside the domain's boundary surfaces (at $i = 0, i = N_i + 1, j = 0, j = N_j + 1, k = 0, k = N_k + 1$) that are used to facilitate the specification of boundary conditions. Each grid cell has an east, west, north, south, top, and bottom face denoted by e, w, n, s, t, b. The ξ, η, σ faces range from $i = 0, \cdots, N_i, j = 0, \cdots, N_j$, and $k = 0, \cdots, N_k$. The flux U is specified on the east and west face, V is specified at the north and south face, and W or $\mathcal{W}$ are specified at the top and bottom face of a cell.

4. Solution procedure

We integrate the advective terms explicitly, but treat the free-surface terms and free-surface equation implicitly so that the surface gravity wave does not govern the time step of integration. This can be done within a third-order Runge Kutta scheme, in which the unconditionally stable implicit procedure shares the same time stages as the explicit one. The time step of integration is thus conveniently based on the fluid velocity. Our numerical procedure combines algorithmic ideas from the fractional step method of Kim and Moin (1985) and the semi-implicit free-surface formulation of Casulli and Cheng (1992); Casulli (1995) while using the numerical framework of Zang et al. (1994). The method used by Dukowicz and Smith (1994) for free-surface calculations is similar to the method that is proposed in Casulli and Cheng (1992) and used here.

The solution procedure for advancing the solution from time step n to $n + 1$ consists of 5 steps (they may be implemented at each stage of a multistage scheme) and are summarized as follows:

1) Compute a preliminary velocity field u^*, v^*, w^* and the final salinity, s^{n+1} and temperature T^{n+1} by explicit advancement of the advective terms based on the solution u^n, v^n, w^n, s^n, T^n at the previous step. Specify temperature and salinity boundary conditions at the inflow. Evaluate the density ρ^{n+1} at the new time step and r^{n+1} by integrating the density from the free surface downward. The free-surface position used is that from the previous time level. Interpolate the preliminary velocities on to cell faces to determine the preliminary fluxes U^*, V^*, $\mathcal{W}^*$ using (3.6) and (3.11).

2) Equations for the predictor horizontal velocities are

$$\tilde{u} = u^* - \Delta t\epsilon^{-1}(gD_x h^{n+1} + D_x r^{n+1} - fv^n + \epsilon\delta b w^n)$$

$$\tilde{v} = v^* - \Delta t\epsilon^{-1}(gD_y h^{n+1} + D_y r^{n+1} + fu^n), \quad (4.1)$$

where D_x, D_y are discrete approximations to ∂_x, ∂_y. (For better accuracy, replace h^{n+1} by the mean of h^n and h^{n+1}.) Write similar equations for the predictor fluxes $\tilde{U}$, $\tilde{V}$, and substituting these into the discretized equation for the free surface (3.12), obtain a 2D elliptic equation for h^{n+1}. Solve this to obtain h^{n+1}. At the boundaries we require $\tilde{U}$ or $\tilde{V}$ summed over the depth as boundary conditions. We assume these to be the same as the final boundary conditions since the contribution of the nonhydrostatic pressure is very small in the horizontal momentum equations.

3) Now compute the predictor velocities $\tilde{u}$, $\tilde{v}$ from u^*, v^*, w^* using (4.1). Also compute the corresponding fluxes $\tilde{U}$, $\tilde{V}$, $\tilde{\mathcal{W}}$ at cell faces.

4) The equations for the final velocities are written as

$$u^{n+1} = \tilde{u} - \Delta t\epsilon^{-1}\delta D_x q^{n+1}$$

$$v^{n+1} = \tilde{v} - \Delta t\epsilon^{-1}\delta D_y q^{n+1}$$

$$w^{n+1} = w^* - \Delta t\beta(D_z q^{n+1} - b\tilde{u}). \quad (4.2)$$

Write corresponding equations for the fluxes U^{n+1}, V^{n+1}, $\mathcal{W}^{n+1}$ and substitute these into the discretized continuity equation (3.10) to obtain a 3D elliptic equation for the nonhydrostatic pressure q^{n+1}. Solve this equation while specifying velocity fluxes at lateral and bottom boundaries and $q^{n+1} = 0$ at the free surface. At the outflow we may specify either the flux or the distribution of pressure q^{n+1}. A reasonable pressure distribution to use is one that results in no vertical acceleration as the fluid exits the domain.

5) Compute the final velocities u^{n+1}, v^{n+1}, w^{n+1} using (4.2) and specify the velocities at the inflow. The corresponding fluxes U^{n+1}, V^{n+1}, $\mathcal{W}^{n+1}$ with their values specified at lateral and solid boundaries satisfy the discrete continuity equation to within a factor of the tolerance set on the residual in the elliptic equation for nonhydrostatic pressure.

The procedure described is conservative in volume and in the scalar quantities such as temperature and salinity. Since we ensure that the volume flux into the domain is equal to the volume flux out of the domain at the predictor step, the mean sea surface elevation remains zero throughout the computation. At each step, the terms on the right-hand side of the elliptic equation for q^{n+1} contain a flux balance across cell faces at the previous step. Hence, each time the residual is fed back into the right-hand side of the elliptic

equation. This ensures that there is no growth in the divergence of the velocity with time. For a more detailed account of the step-by-step solution procedure see Mahadevan (1995).

5. Solution of the elliptic pressure equation in curvilinear coordinates

The solution of the elliptic pressure equation in three-dimensions is computationally the most expensive step in the solution procedure. We find that it is possible to greatly speed up the solution by (i) using the multigrid technique and (ii) making use of the free-surface formulation to decouple the pressure into hydrostatic and nonhydrostatic components, and then taking advantage of the inhomogeneity in the nonhydrostatic pressure equation.

a. Multigrid solution technique

The transformation from curvilinear coordinates results in the coefficients in the elliptic difference operator varying with each grid cell. This precludes the use of direct solvers for the elliptic equation. We thus resort to the multigrid technique (Brandt 1984), which has been shown to work well in the case of curvilinear coordinates by Perng (1990) and Zang et al. (1994). The solver we have developed uses a V cycle with Gauss Seidel relaxation at each level.

b. Advantages of the free-surface formulation

In the free-surface model, the pressure at the free surface is specified as a Dirichlet boundary condition. The linear system arising from the discretization of the elliptic equation for pressure is positive definite and has better properties than the singular system that results from the corresponding rigid-lid problem with flux boundary conditions.

There is a second more distinct advantage to the free-surface formulation in the model where we modify the hydrostatic balance. This arises from the fact that the coefficients on the vertical arm of the difference stencil are 1 or 2 orders of magnitude larger than the other coefficients. Three of the diagonals in the matrix of the linear system are therefore much more dominant than the others. The variation of the second derivative of the nonhydrostatic pressure is very small in the vertical as compared to the horizontal direction, and the system can be solved very rapidly using line by line relaxation in the vertical. To illustrate why this is so, we consider the solution of the dimensionless form of the equations on a rectilinear grid using a simple time integration scheme to advance the solution from time step n to $n + 1$. If the final velocities are computed using

$$u^{n+1} = \tilde{u} - \Delta t \epsilon^{-1} \delta D_x q^{n+1}$$

$$v^{n+1} = \tilde{v} - \Delta t \epsilon^{-1} \delta D_y q^{n+1}$$

$$w^{n+1} = w^* - \Delta t \beta (D_z q^{n+1} - b\tilde{u}), \qquad (5.1)$$

where Δt is the time step; D_x, D_y, D_z are discrete approximations to ∂_x, ∂_y, ∂_z; Δx, Δy, Δz are dimensionless grid spacings in the x, y, z directions; and the fluxes defined as $U = u\Delta y \Delta z$, $V = v\Delta x \Delta z$, $\mathcal{W} = \epsilon w \Delta x \Delta y$ are computed as

$$U^{n+1} = \tilde{U} - \Delta t \epsilon^{-1} \delta D_x q^{n+1} \Delta y \Delta z$$

$$V^{n+1} = \tilde{V} - \Delta t \epsilon^{-1} \delta D_y q^{n+1} \Delta x \Delta z$$

$$\mathcal{W}^{n+1} = \tilde{\mathcal{W}} - \Delta t \epsilon \beta (D_z q^{n+1} - b\tilde{u}) \Delta x \Delta y, \qquad (5.2)$$

then the discrete elliptic equation formed by substituting the above fluxes into the discrete continuity equation (3.10), using central differencing and assuming all the dimensionless grid spacings equal Δ is

$$\left\{ (q_{i+1} - 2q_i + q_{i-1}) + (q_{j+1} - 2q_j + q_{j-1}) + \frac{\epsilon^2 \beta}{\delta} (q_{k+1} - 2q_k + q_{k-1}) \right\}^{n+1}$$

$$= \frac{1}{\Delta t} \frac{1}{\Delta} \frac{\epsilon}{\delta} (\tilde{U}_e - \tilde{U}_w + \tilde{V}_n - \tilde{V}_s + \tilde{\mathcal{W}}_t - \tilde{\mathcal{W}}_b) + \frac{\epsilon^2 \beta}{\delta} ([b\tilde{u}]_t - [b\tilde{u}]_b) \Delta. \qquad (5.3)$$

The subscripts n, s, e, w, t, b on a quantity indicate the cell face at which it is specified, and the square brackets indicate interpolation on to a cell face.

We see that, if $\epsilon^2 \beta / \delta = 1$, the diagonals of the matrix of the linear system are -1, -1, -1, -1, -1, -1, 6. On the other hand, if $\epsilon^2 \beta / \delta = 10$, the diagonals are -1, -1, -1, -1, -10, -10, 24 and the system can be solved much faster than the previous one by using block relaxation, which is equivalent to line by line relaxation in the vertical. Thus, it is a great numerical advantage if $\epsilon^2 \beta / \delta \gg 1$.

In the case of the rigid-lid formulation, the vertical momentum equation is given by

$$\frac{Dw}{Dt} + \alpha_1 (p_z + \rho g - \delta b u) = 0, \qquad (5.4)$$

where α_1 replaces the coefficient $1/\epsilon^2 \delta^2$ in the exact equations (Mahadevan et al. (1996). The hydrostatic balance is not subtracted out in this case, since the total

pressure p is not decomposed into hydrostatic and nonhydrostatic components. The discrete elliptic equation for pressure formed from the continuity equation is then

$$\{(p_{i+1} - 2p_i + p_{i-1}) + (p_{j+1} - 2p_j + p_{j-1}) + \epsilon^2\alpha_1 (p_{k+1} - 2p_k + p_{k-1})\}^{n+1}$$
$$= \frac{1}{\Delta t}\frac{\epsilon}{\Delta}(U_e^* - U_w^* + V_n^* - V_s^* + W_t^* - W_b^*) + \epsilon^2\alpha_1([\rho g]_t - [\rho g]_b) + \cdots \text{Coriolis terms.} \quad (5.5)$$

The numerical solution of this system could be speeded up if $\epsilon^2\alpha_1$ were large, but it is not.

In the above equations, we wish to make α_1 and β as small as possible to alleviate the problem of insufficient accuracy encountered when computing the difference of the pressure gradient and buoyancy terms in the exact vertical momentum equation. Yet, α_1 and β must be kept larger than a certain minimum value in order that the solution of the modified equations does not differ from that of the original equations by more than a certain permissible amount. A value of 100 for both α_1 and β maintains two digits of solution accuracy. The free-surface formulation is much more advantageous than the rigid-lid one because a larger value of the coefficient in the pressure equation can be achieved while keeping α_1 and β as small as possible. Table 1 illustrates this. When $\epsilon = 0.1$, we get almost an order of magnitude speedup in the numerical solution by going from the rigid-lid to the free-surface formulation.

Thus, we have seen that it is possible to take advantage of the inhomogeneity in the elliptic pressure equation with the free-surface formulation. The free-surface formulation also has the advantage of a Dirichlet boundary condition at the free surface.

It is worth noting that in the original nonhydrostatic equations, that is, the equations without the approximation that permits an exaggerated deviation from hydrostatic balance, the value of the crucial coefficient in the 3D elliptic pressure equation would be $1/\delta^2$, irrespective of whether the equation were for the total pressure or merely its nonhydrostatic component. This is apparent if we recollect that in the approximation, α_1 and β replaced the coefficients $1/\epsilon^2\delta^2$ and $1/\epsilon^2\delta$. The large value of $1/\delta^2$ that results from the shallowness of the fluid also implies near hydrostatic balance. For the same reason, however, the original equations prove to be difficult in the integration of the vertical momentum equation and we cannot use them even though solving the elliptic pressure equation would be easy.

Solving the elliptic pressure equation with Neumann boundary conditions in this framework is peculiar due to the fact that the grid is not orthogonal to the boundary. Since the specification of the normal derivative at a boundary involves cross-derivative terms, points outside the boundary cannot be eliminated explicitly from the system. They must ideally be included in the vector of unknowns when solving the linear system arising from the discretized elliptic equation. If, however, a Dirichlet boundary condition is prescribed at a cell face as being the mean of two adjacent cell values, then the point outside the boundary must be eliminated from the vector of unknowns. If included, the matrix of the linear system is no longer positive definite and convergence is not achieved by common iterative methods. Alternatively, solving a linear system for the values in the interior of the domain, and using the boundary conditions to update the points outside the boundary with each iteration also works.

When the grid cells along a boundary are skewed, the off-diagonal metric terms in the Jacobian matrix are large. If the cross-derivative terms exceed the across-boundary derivative terms that comprise the normal derivative at a boundary, then using the Neumann boundary condition is problematic. Convergence is not achieved because the normal derivative in physical space lies more along the tangential direction in computational space. Grid skewness at the boundary that results when steep topography intersects a lateral boundary or when the domain is complicated in shape should therefore be minimized.

6. Modeling the circulation in the Gulf of Mexico

We now use the numerical model based on the quasi-nonhydrostatic equations to simulate the flow in a nat-

TABLE 1. Possible values of the coefficient in the elliptic equation.

		Value of coefficient when	
	Coefficient	$\epsilon = 10^{-1}, \alpha_1 = 10^2, \beta = 10^2$	$\epsilon = 10^{-2}, \alpha_1 = 10^3, \beta = 10^3$
Free-surface model	$\epsilon^2\beta/\delta$	100	10
Rigid-lid model	$\epsilon^2\alpha_1$	1	0.1

ural ocean basin: the Gulf of Mexico. Our objective is to demonstrate the use of the model by simulating the circulation pattern, and we have not attempted to use real data to simulate a particular period in the history of the gulf, nor have we used wind stresses, heat, or salt fluxes at this stage. Since the equations are well posed, we model the gulf without additional buffer regions at open boundaries, and with either no viscous dissipation term or one that is very small.

The Gulf of Mexico is a more or less enclosed basin situated between 18° and 31°N, 80° and 98°W. It is connected to the Caribbean Sea through the Yucatan Channel and to the Atlantic Ocean through the Straits of Florida. The Gulf Stream, which enters through the Yucatan Channel and leaves through the Florida Straits, drives the circulation in the basin. The gulf has a shallow shelf less than 500 m in depth (see Fig. 1) that extends out several hundred kilometers from the shore before the ocean bed plunges to depths as deep as 3500 m.

Modeling an ocean region requires data at open boundaries and the data required depends on whether there is inflow or outflow at the boundary. In the Gulf of Mexico there is predominantly inflow through the Yucatan Channel and outflow through the Straits of Florida. The channel fluxes are estimated to be about 30 Sv (1 Sv $\equiv 10^6$ m^3 s^{-1}). Earlier numerical studies, for example, Hurlburt and Thompson (1980), reveal that the gulf circulation is not significantly affected by small variations in the inflow nor by winds. Hence, it is possible to model the gulf circulation quite realistically without using very specific time-dependent boundary conditions.

a. Observed circulation in the gulf

Studies of the gulf's circulation by Vidal et al. (1994), Hofmann and Worley (1986), Elliott (1982), and Lewis and Kirwan (1985) have shown that it is predominated by an anticyclonic (clockwise) circulation that intensifies into a western boundary current along the western margin. In the east, the inflow evolves into the Loop Current, which exits through the Straits of Florida. The intrusion of the Loop Current varies with time, and periodically (about once or twice a year) the loop folds back on itself and gets pinched off to form an anticyclonic ring. Such rings typically have diameters of 200–300 km and drift westward at approximately 2 km day^{-1}. The Loop Current rings carry a warm and salty core of Caribbean water and leave an identifiable signature in the isotherm and isohaline lines. The rings persist from several months to

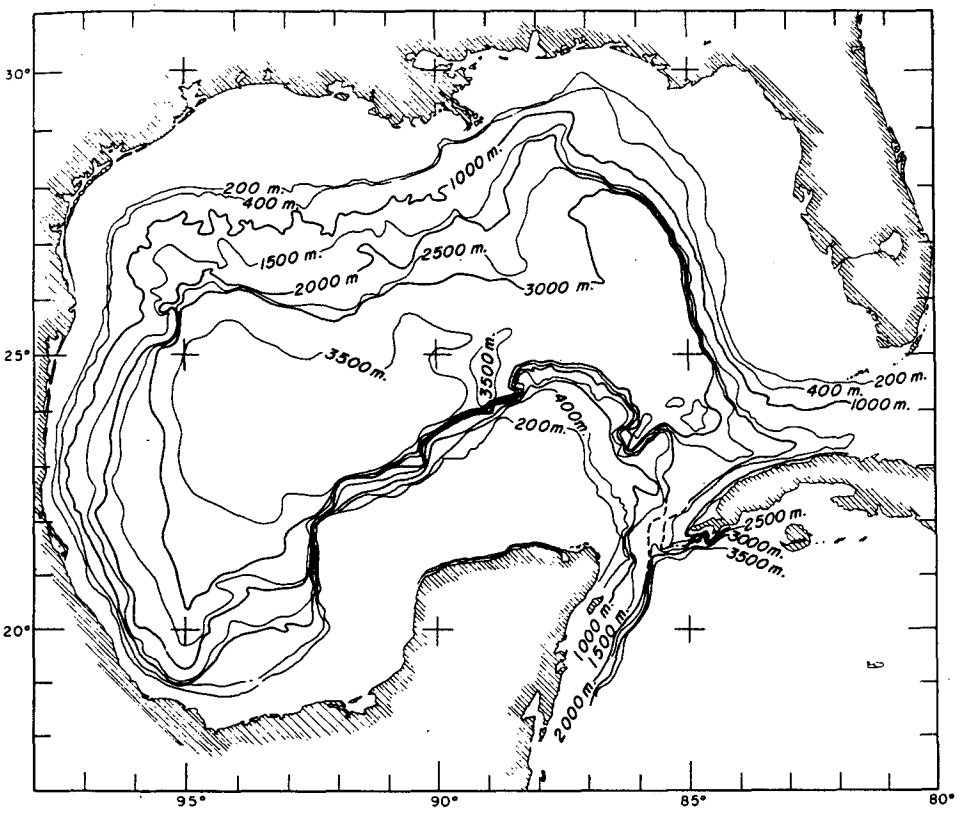

FIG. 1. Bathymetry of the Gulf of Mexico.

a year. Besides the rings pinched from the Loop Current, there are several other cyclonic and anticyclonic eddies generated by topography or other factors. More recently, cyclonic–anticyclonic pairs of eddies have been observed in the western gulf.

The Loop Current and western boundary current can be easily observed in the top 200–500 m of the gulf where their intensity is maximum. There is comparatively little observation of the deep circulation in the gulf and current meter readings are scarce. Molinari et al. (1978) claim the existence of a deep anticyclonic gyre similar to what exists in the upper layers, while Hofmann and Worley (1986) cite evidence for the deep circulation to be a cyclonic gyre, opposite in direction to the anticyclonic circulation in the upper layers.

b. *Geometric modeling of the physical domain*

The lateral boundaries of the domain are formed by the coastline of the gulf, the 21.5°N latitude through the Yucatan Channel and the 81°W longitude through the Straits of Florida. We approximate shallow coastal areas that are less than 500 m deep to have a constant depth of 500 m and model the coast as a vertical wall.

The plan view of the Gulf is mapped onto a square that is one face of our computational domain. The vertical lateral boundaries form the four lateral faces and the ocean bed forms the bottom face. In the plan view (see Fig. 2), the lateral boundary of the domain is comprised of four boundary curves, each a parametric B spline that has been fitted to data. Boundary curves 1 and 3 are described by parameter $\xi \in [0, N_i]$, and boundary curves 2 and 4 by parameter $\eta \in [0, N_j]$, where N_i and N_j are the number of grid intervals in the ξ and η directions respectively.

Boundary curves 1, 2, 3, 4 are discretized, and a grid is generated on the top boundary face using the grid generation program of Venkata (1991) that uses transfinite interpolation to compute the interior points from the boundary curves. Since we use a sigma coordinate, the grid from the top surface is simply repeated at each σ level in the domain.

The bathymetric data is extracted from the database ETOPO5 (at the National Center for Atmospheric Research), modified so that any elevation greater than -500 m in our ocean domain is changed to -500 m, and fitted with a bicubic B spline using the B spline library in INTEGRA 3.2 (Pereyra 1990). The bicubic B spline describes the surface topography as a continuous function $d = d(\theta, \phi)$ of longitude and latitude and makes available the derivatives d_θ, d_ϕ.

In the vertical, we divide the total depth of fluid at any point into N_k equal layers. The layer interfaces are surfaces of constant σ value and range from $\sigma = 0$ at the ocean bottom to $\sigma = N_k$ at the free surface.

c. *Initial and boundary conditions for the Gulf of Mexico*

A two-dimensional geostrophic flow could be used as the initial condition when the domain bottom is flat. When the topography varies, we start the flow from rest

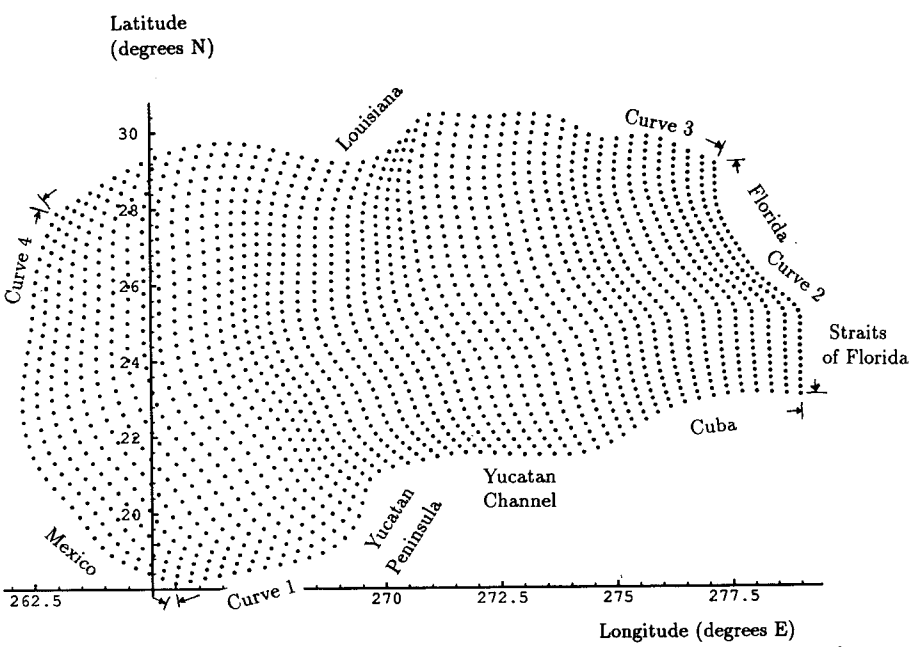

FIG. 2. Plan view of the grid for the Gulf of Mexico.

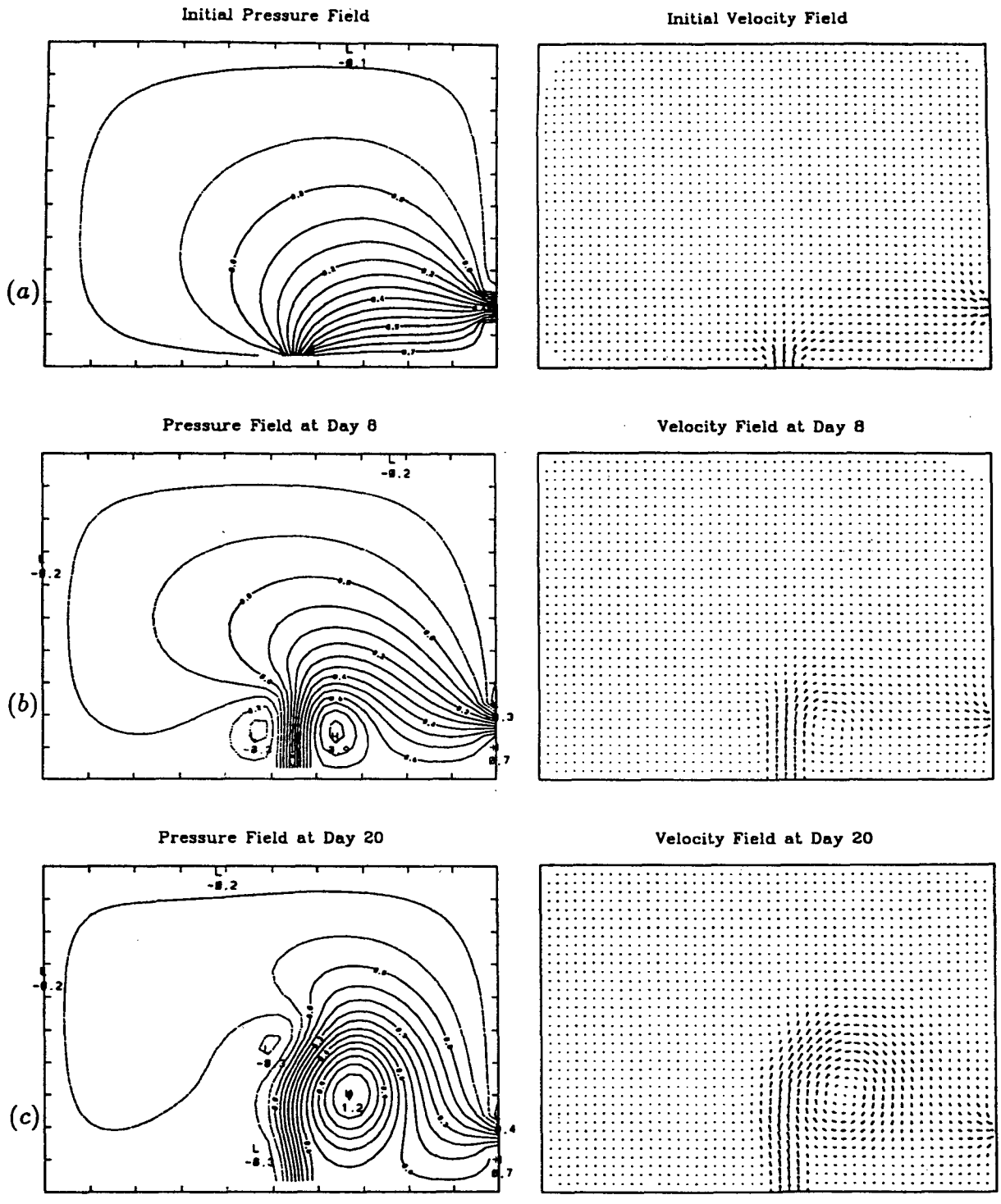

FIG. 3. Numerical rigid-lid simulation of the Loop Current and eddy shedding in a rectangular basin. The domain is 400 km × 600 km × 1000 m. The fluid is homogeneous with no variation of the flow in the vertical. The plots (a–f) show a progression in time of the pressure and horizontal velocity fields at the 500-m level.

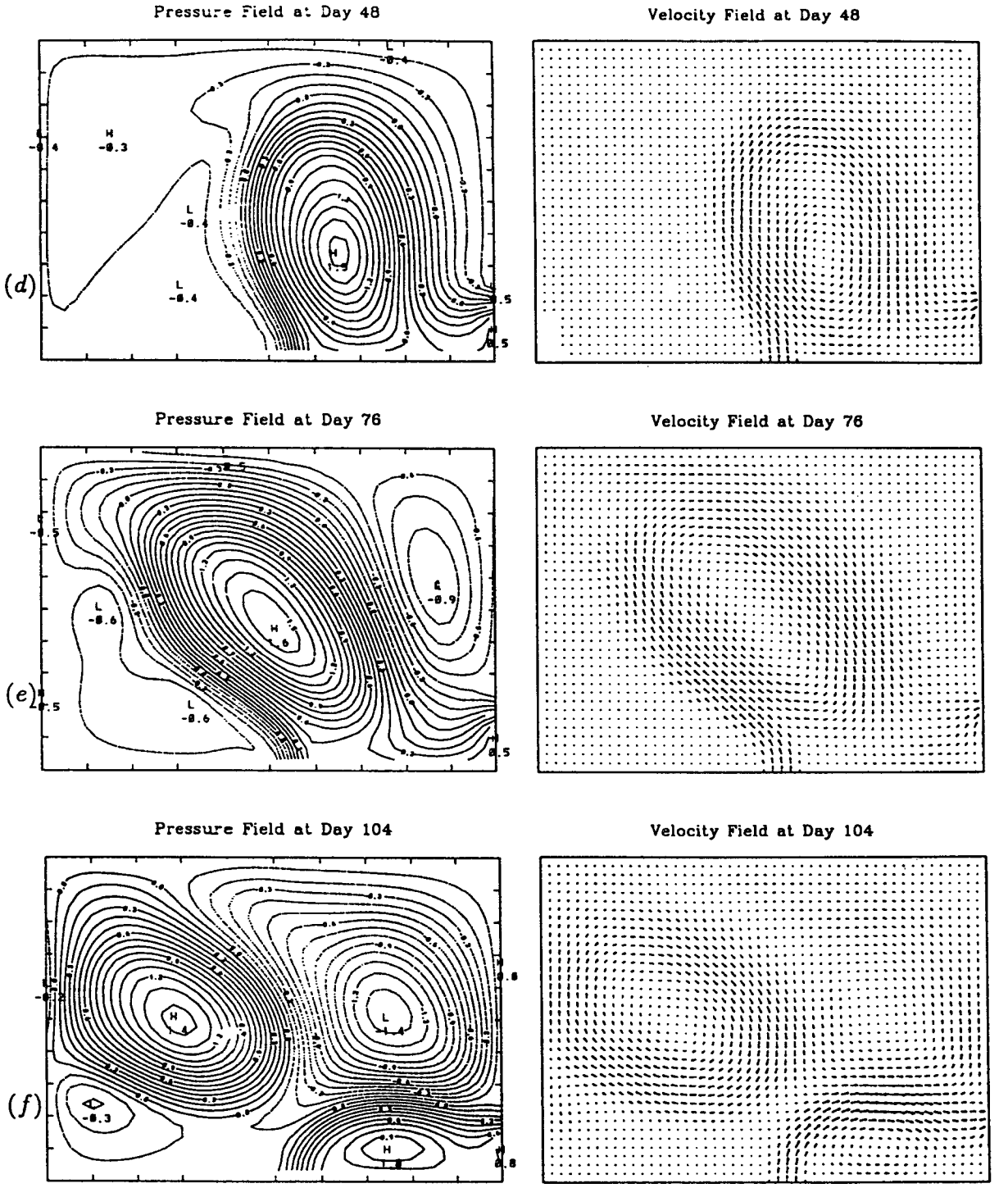

FIG. 3. (*Continued*)

and linearly ramp the inflow velocities over 100 time steps to represent those in the Yucatan Channel. The inflow profile is estimated from data published by Boisvert (1967), which shows the maximum current velocity through the Yucatan to be approximately 0.93 m s^{-1}. We vary the velocity with depth so that it is small at the bottom of the channel. At the outflow we prescribe a parabolic velocity profile that is gradually

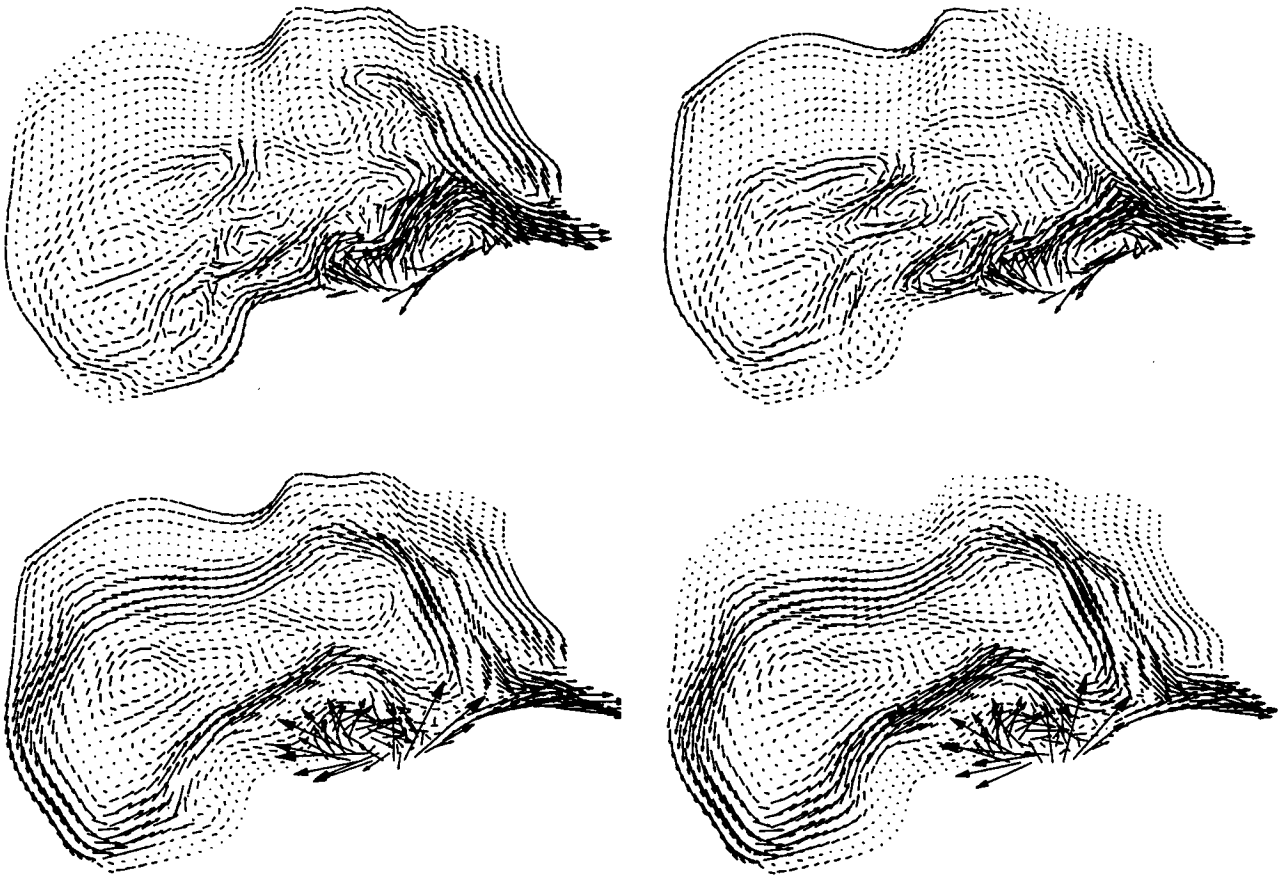

FIG. 4. Numerical simulation of the Gulf of Mexico. The horizontal velocity field is plotted on a sigma surface. The top panel shows a surface (layer 15) near the top. The bottom panel shows a surface (layer 2) close to the bottom that follows the topography. (a) day 104, time step: 3000; (b) day 208, time step: 6000;

allowed to adjust with the constraint that the net outflow equals the net inflow into the gulf. This is a reasonable assumption given that the mean sea level does not fluctuate very much in the gulf.

The Atlantic temperature and salinity data from Levitus (1982) is interpolated to specify initial S and T fields that vary with latitude and depth. The initial values are held constant at the inflow over time.

Surface heat and salt fluxes are not included in the model at the present but could be included for a more realistic picture of the salinity and temperature fields. Wind stress, river inflows, and seasonal variations in the Yucatan inflow are also neglected for the present as their contribution to the mesoscale circulation in the gulf is believed to be small.

d. Model parameters

Since the maximum Loop Current velocities are approximately 1.5 m s^{-1}, we choose $U = 1$ m s^{-1} as the characteristic velocity. The characteristic length scale L of the eddies is 100 km, and since the rotation rate parameter $F = 10^{-4}$ s^{-1}, the Rossby number $\epsilon \equiv U/FL = 10^{-1}$. The characteristic free-surface elevation H turns out to be 1 m for these parameters assuming that the free-surface pressure gradient and Coriolis forces are approximately in balance. The depth scale D is 1000 m and the aspect ratio $\delta \equiv D/L = 10^{-2}$. We would like to use a horizontal resolution of approximately 10 km to resolve 100 km flow features in the horizontal, and a vertical resolution of about 100 m in the deepest parts. However, we could not afford this resolution for the entire gulf on the multiprocessor work-station we used for the simulations, and hence used a coarser mesh of $48 \times 32 \times 16$ grid cells with an approximate resolution of 40 km $\times$ 40 km in the horizontal and 200 m at maximum in the vertical. The vertical grid spacing varies with the depth of the ocean, being maximum in the deepest portions and minimum on the shelf regions. We set the relaxation parameter β in the vertical momentum equations to be 100 in order to maintain two digits of solution accuracy. We verify that the results are not sensitive to this particular choice of β, by com-

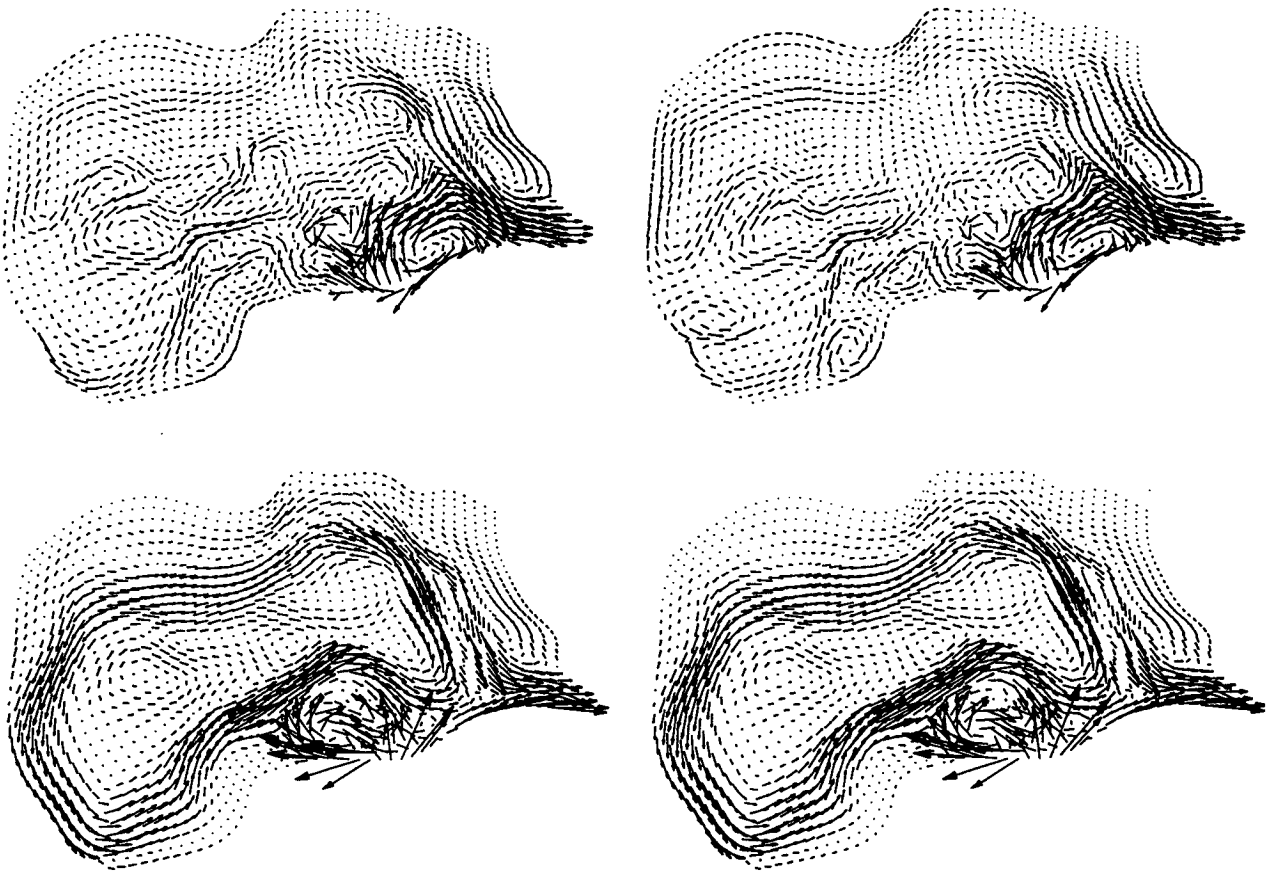

FIG. 4. (*Continued*) (c) day 312, time step: 9000; and (d) day 416, time step: 12 000.

paring results obtained with $\beta = 100$ to those for $\beta = 50$, 25, and 12.5.

7. Analysis of the model

Before describing our numerical experiments, we present some analysis to motivate the experiments and to help understand the observations. We also examine some of the consequences of our approximations.

a. Modification of the internal gravity wave speed

The model permits a greater deviation from hydrostatic balance than what exists in the ocean. The dimensionless equation for vertical momentum prior to making any approximation is

$$\frac{Dw}{Dt} + \frac{1}{\epsilon^2\delta^2}\left(p_z + \rho g - \delta bu - \lambda\epsilon\delta\frac{(u^2 + v^2)}{a}\right) = 0, \quad (7.1)$$

where p_z is the vertical pressure gradient. The large coefficient $1/\epsilon^2\delta^2$ in the above equation is replaced by α_1 in the model without free surface, where $\alpha_1 \ll 1/\epsilon^2\delta^2$.

The external gravity waves are not affected by this approximation as the free-surface pressure gradient contributes only to the horizontal momentum equations, which are unaltered by the approximation. Let γ denote the ratio of the the coefficient $1/\epsilon^2\delta^2$ that multiplies the pressure gradient and gravity terms in the exact vertical momentum equation to its modified value α_1. In the case that $\epsilon = 10^{-1}$, $\delta = 10^{-2}$ and $\alpha_1 = 100$, $\gamma = 10^4$. If we neglect the effect of the earth's rotation and linearize the equations about a state of rest, the dispersion relation for internal gravity waves in a continuously stratified ocean as derived by Gill (1982) is

$$\omega^2 = (k^2 + l^2)N^2/(k^2 + l^2 + m^2). \quad (7.2)$$

Here ω is the frequency of the internal gravity waves, (k, l, m) is the wavenumber vector, and N^2 is the buoyancy frequency defined by $N^2 = -g\rho_0^{-1}d\rho_0/dz$, where $\rho_0(z)$ is mean density profile. The ratios k/m and l/m are $O(\delta)$ for the cases of interest to us. Dividing numerator and denominator by m^2, we observe that, since $\delta \ll 1$,

$$\omega^2 \approx 2\delta^2N^2/(2\delta^2 + 1) \approx 2\delta^2N^2.$$

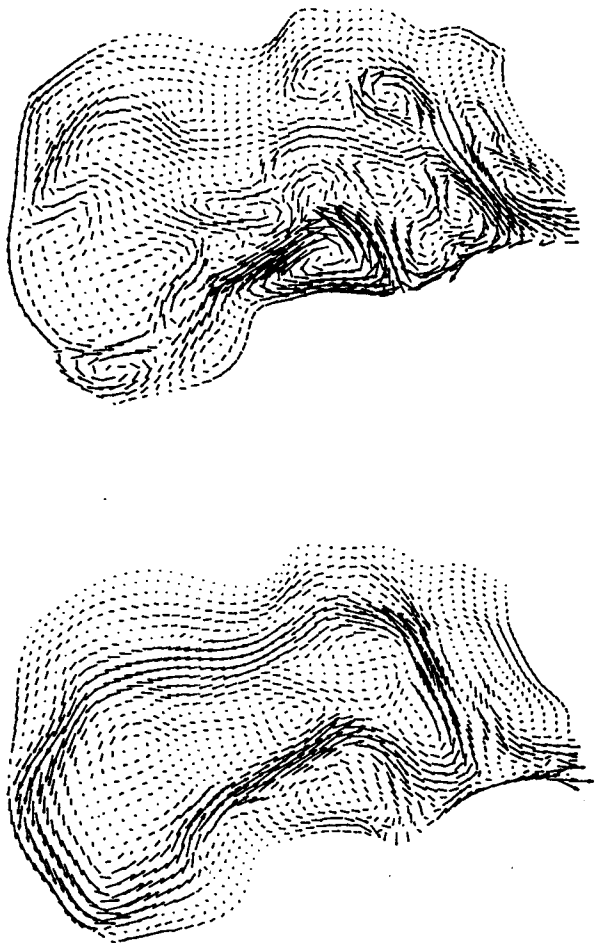

FIG. 5. Numerical simulation of the Gulf of Mexico with viscosity ($\nu_H = 100$ m^2 s^{-1}, $\nu_V = 10^{-4}$ m^2 s^{-1} and bottom drag. The horizontal velocity field is plotted on a sigma surface at day 312, time step = 9000. The top panel shows a surface (layer 15) near the top. The bottom panel shows a surface (layer 2) close to the bottom that follows the topography.

By permitting a greater deviation from hydrostatic balance in the equations, the dispersion relation is altered to

$$\begin{aligned}\omega^2 &= (k^2 + l^2)N^2/(\gamma k^2 + \gamma l^2 + m^2)\\ &\approx 2\delta^2 N^2/(2\delta^2\gamma + 1)\\ &= 2\delta^2 N^2/3\end{aligned}$$

when

$$\gamma = 10^4, \quad \delta = 10^{-2}. \tag{7.3}$$

Hence, we see that changing the coefficient $1/\epsilon^2\delta^2$ to α_1 in the equations reduces the frequency and consequently the phase speed and group velocity of the internal gravity waves approximately by a factor of $(2\delta^2\gamma + 1)^{1/2}$, where $\gamma \equiv (1/\epsilon^2\delta^2)/\alpha_1$. This factor is $\sqrt{3}$ in the above example.

b. Inclusion of the Coriolis term in the vertical momentum equation

We have seen from the scaling in Mahadevan et al. (1996) that the Coriolis term due to the tangential component of the earth's rotation that appears in the vertical momentum equation cannot be neglected in the nonhydrostatic equations. The equations for generation of horizontal vorticity in the x and y directions are written in dimensionless form as

$$\begin{aligned}&\frac{\partial\zeta_1}{\partial t} + \beta(q_{zy} - bu_y - b_y u) - \epsilon^{-1}\\ &\qquad\times[(p_h + \delta q)_{yz} + fu_z] = 0\\ &\frac{\partial\zeta_2}{\partial t} - \beta(q_{zx} - bu_x) + \epsilon^{-1}[(p_h + \delta q)_{xz} - fv_z] = 0,\end{aligned} \tag{7.4}$$

where $\zeta_1 \equiv w_y - v_z$ and $\zeta_2 \equiv u_z - w_x$. The first-order nonlinear terms have been neglected in these equations. The horizontal gradient of $(q_z - bu)$ generates horizontal vorticity that manifests itself as circulation cells in the vertical.

c. Generation of vertical vorticity

The dimensionless equation for vertical vorticity $\zeta \equiv v_x - u_y$ formed by cross differentiating and subtracting the horizontal momentum equations is

$$\begin{aligned}&\frac{D\zeta}{Dt} + \epsilon(w_x v_z - w_y u_z)\\ &\qquad + \left(\frac{1}{\epsilon}f + \zeta\right)(u_x + v_y) + \frac{\lambda}{\epsilon}\frac{bv}{a} = 0.\end{aligned} \tag{7.5}$$

On neglecting terms less than or equal to $O(\epsilon)$, the above equation reduces to

$$\frac{D\zeta}{Dt} + \frac{1}{\epsilon}f(u_x + v_y) + \frac{\lambda}{\epsilon}\frac{bv}{a} = 0. \tag{7.6}$$

Here $(u_x + v_y)$ is $O(\epsilon)$, and its product with f is referred to as vorticity stretching. The term $\epsilon^{-1}\lambda bv/a$ results from the variation of the vertical planetary vorticity with latitude and is derived as

$$\epsilon^{-1}f_y v = \epsilon^{-1}f_\phi\phi_y v = \epsilon^{-1}\lambda bv/a, \tag{7.7}$$

where λ is the ratio of the length scale to characteristic distance to the earth's center, taken as 10^7 m, and b, v, a are dimensionless. If $L = 10^5$ m, $U = 1$ m s^{-1}, then $\lambda = 10^{-2}$, $\epsilon = 10^{-1}$, and the term $\epsilon^{-1}f_y v$ is $O(10^{-1})$.

When the ocean bottom is flat and the flow is more or less two-dimensional, vortex stretching is small and the variation of the Coriolis parameter f along a northward trajectory imparts negative vorticity to the flow. This is responsible for the clockwise looping of the Loop Current. When there are variations in topography,

$(u_x + v_y) = O(\epsilon)$, and the $O(1)$ vortex stretching term becomes the dominant vorticity generation mechanism.

d. Estimation of Loop Current intrusion and eddy size using the theory of potential vorticity conservation

The competing effects of topography and latitudinal variation of f on the Loop Current can be examined using the equation for the conservation of potential vorticity

$$\frac{D}{Dt}\left(\frac{f+\zeta}{d+h}\right) = 0, \tag{7.8}$$

where $d + h$ is the total depth of fluid. An increase in depth as the jet moves northward from the entrance of the gulf results in positive vorticity that counters the negative vorticity induced due to an increase in f.

Hurlburt and Thompson (1980) and Reid (1972) estimate the Loop Current intrusion and the size of the shed eddy from the theory of potential vorticity conservation. Assuming a parcel to be moving at constant velocity u_c along the current core and neglecting the effects of topography, the northward intrusion of the Loop Current just before the pinching of an eddy is estimated in terms of dimensional quantities as

$$l = \left(\frac{2u_c a}{2\Omega \cos\phi}(1 - \cos\phi_0)\right)^{1/2}, \tag{7.9}$$

where a denotes the earth's radius, ϕ the latitude, and ϕ_0 the mean latitude about which the latitudinal variation is linearized. The north–south extent of the loop l, and the size of the eddy in the Gulf of Mexico is estimated to be about 220 km by Reid (1972) and is in agreement with our numerical observations in a flat-bottomed rectangular basin (section 8a).

e. Effect of topography

In order to quantify the effect of topographic variations we combine the vertical vorticity equation (7.6) with the equation of continuity integrated over depth. If the free-surface elevation is nondimensionalized by the total depth, that is, $h = h'D$, then the dimensionless equation of continuity for a column of fluid is

$$\frac{\partial h}{\partial t} + \frac{\partial}{\partial x}\int_{-d}^{h} u\,dz + \frac{\partial}{\partial y}\int_{-d}^{h} v\,dz = 0. \tag{7.10}$$

Rewriting this equation as

$$\frac{\partial h}{\partial t} + \int_{-d}^{h}(u_x + v_y)dz + u(z=h)\frac{\partial h}{\partial x} + v(z=h)\frac{\partial h}{\partial y} + u(z=-d)\frac{\partial d}{\partial x} + v(z=-d)\frac{\partial d}{\partial y} = 0 \tag{7.11}$$

and combining it with the vertically integrated vorticity equation (7.6) gives

$$\int_{-d}^{h}\frac{D\zeta}{Dt}dz - \frac{f}{\epsilon}\left(u(z=-d)\frac{\partial d}{\partial x} + v(z=-d)\frac{\partial d}{\partial y} + \frac{\partial h}{\partial t} + u(z=h)\frac{\partial h}{\partial x} + v(z=h)\frac{\partial h}{\partial y}\right) + \frac{\lambda}{\epsilon}\frac{b}{a}\int_{-d}^{h} v\,dz = 0. \tag{7.12}$$

Since h is not $O(1)$ but is $O(H/D)$ here, the terms containing the partial derivatives of h are negligibly small. Neglecting these, the equation simplifies to

$$\int_{-d}^{h}\frac{D\zeta}{Dt}dz - \frac{f}{\epsilon}\left(u(z=-d)\frac{\partial d}{\partial x} + v(z=-d)\frac{\partial d}{\partial y}\right) + \frac{\lambda}{\epsilon}\frac{b}{a}\int_{-d}^{h} v\,dz = 0. \tag{7.13}$$

The last term on the left-hand side is $O(10^{-1})$ when $\epsilon = 10^{-1}$, $\lambda = 10^{-2}$. Therefore, it must be that

$$u(z=-d)d_x + v(z=-d)d_y \leq O(\epsilon), \tag{7.14}$$

which explains why the bottom flow closely follows the topographic contours.

The above equation suggests that the topographic steering of the flow may be weakened if the abyssal velocities are themselves negligible. This raises the question as to whether the presence of a boundary layer in the model could change the interior flow field.

8. Numerical experiments

Described below are a few of the numerical experiments performed with the model in trying to understand the circulation in the Gulf of Mexico.

a. Eddy shedding in a rectangular domain

Our first experiment is to simulate a "Loop Current" that sheds eddies. We use a 600 km × 400 km rectangular basin centered at 25°N with a uniform depth of 1000 m and a rigid lid at the top. The basin has an inflow on the southern boundary and outflow on the eastern boundary where we specify parabolic velocity profiles. The fluid is homogeneous, with no density stratification or velocity variation in the vertical. There are no viscous terms in the equations. We use a geostrophic flow as the initial condition. The grid is uniform with 48 × 36 × 10 grid cells and the time step is 30 minutes.

Over a 120-day period we observe the formation of a Loop Current and an eddy. The intrusion of the loop grows

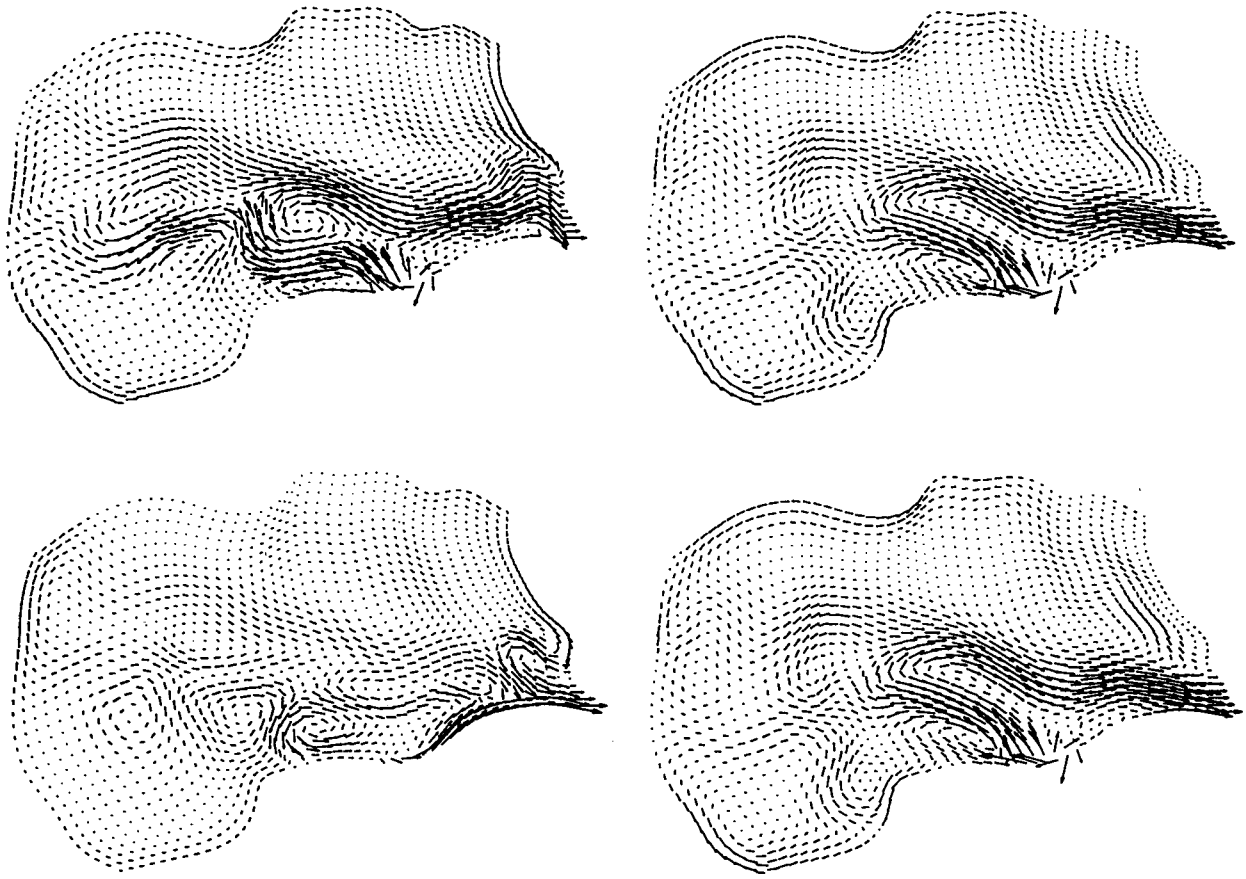

FIG. 6. Numerical simulation of the flat-bottomed basin shaped like the Gulf of Mexico. The horizontal velocity field is plotted on a sigma surface. The top panel shows a surface (layer 15) near the top. The bottom panel shows a surface (layer 2) close to the bottom. (a) day 104, time step: 3000; (b) day 208, time step: 6000;

until it becomes ox-bow shaped and pinches off into a large anticyclonic eddy. As soon as the eddy is detached, the flow short circuits its course directly from the entrance to the exit. Once again, the Loop Current begins to grow and repeat the process. Figure 3 illustrates this.

From these observations we infer that the eddy shedding can occur independent of any baroclinic effects in this geometry. The retroflection of the Loop Current and formation of the eddy is due to the latitudinal variation of the Coriolis parameter and is explained from potential vorticity conservation. The extent of the loop's intrusion and size of the eddy are independent of the domain size as shown by Hurlburt and Thompson (1980) and Reid (1972), provided the distance between the entrance and exit is sufficient to accommodate the loop. The size of the eddy generated in the numerical experiments is consistent with the size estimated from potential vorticity conservation theory.

b. The Gulf of Mexico

We simulate the Gulf of Mexico using a 48 × 32 × 16 size of grid. The grid spacing is thus 40–50 km in the horizontal. In the vertical, it ranges from a minimum of 31.25 m on the 500-m-deep shelf to approximately 220 m in the deepest portion. This resolution is not sufficient to resolve 100 km and smaller eddies and the flow in the narrow inflow region, but can resolve the Loop Current and other features of the general circulation. The horizontal momentum equations contain no viscous terms. We use a fourth-order Shapiro (1970) filter on the vertical velocities every 25 time steps. A time step of 50 minutes is used in the integration.

The flow observed over a period of approximately 400 days shows a general anticyclonic circulation with several eddies forming in the central and western gulf. Tonguelike intrusions of the Loop Current get detached to form eddies that drift westward. Several eddies are seen to form in cyclonic–anticyclonic pairs. The flow distinctly follows the contours of the topography, especially where topographic gradients are steep. A striking feature is the presence of a cyclonic circulation in the deeper layers of the gulf that follows the topographic contours very closely and is opposite in direc-

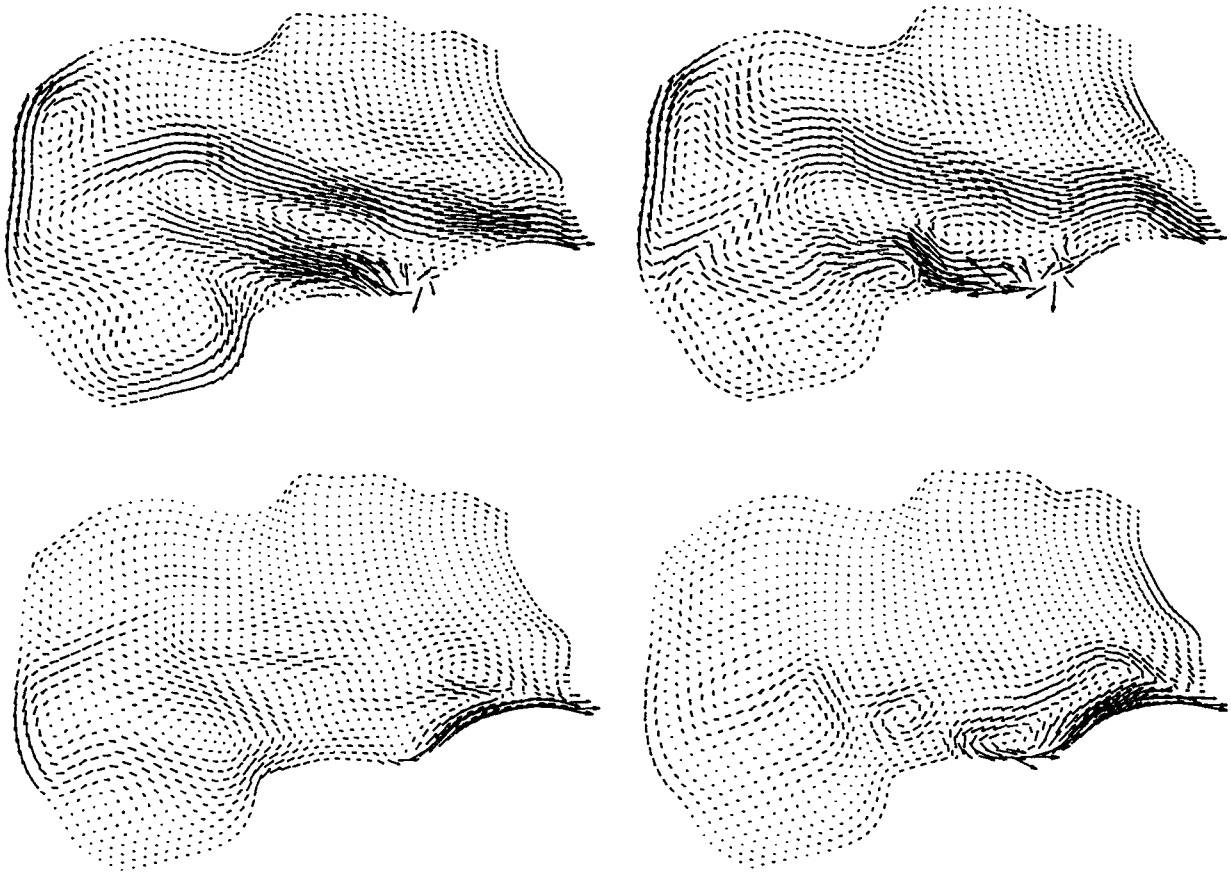

FIG. 6. (*Continued*) (c) day 312, time step: 9000; and (d) day 416, time step: 12 000.

tion to the anticyclonic cell in the upper ocean. Figure 4 shows the development of this flow.

We repeat the above simulation with eddy viscosity terms in the momentum equations and a boundary condition that models the topographic drag. The eddy viscosities used, $\nu_H = 100\ m^2\ s^{-1}$ in the horizontal direction and $\nu_V = 10^{-4}\ m^2\ s^{-1}$ in the vertical direction, are the same as those used by Dietrich and Lin (1994). It is common to use horizontal and vertical eddy viscosities that are 10^{10}–10^{11} and 10^2–10^3 times the molecular viscosity (cf. section 4.6 of Gill 1982). The values used here are 10^8 and 10^2 times the molecular value and are considered relatively small. The bottom drag is modeled as in Casulli and Cheng (1992) using the boundary condition

$$\nu_V \partial u/\partial z = \gamma u \quad \nu_V \partial v/\partial z = \gamma v,$$

where $\gamma = g\sqrt{u^2 + v^2}/C_z^2$ and the Chezy coefficient C_z is given by $C_z = (h + d)^{1/6}/n$. Here $h + d$ is the total depth and n, which is Manning's constant, lies in the range 0.01–0.02.

The circulation generated in this simulation resembles the case without drag in which the difference is that the flow is a little subdued and the Loop Current intrusion less distinct. Figure 5 shows the results from the simulation with the drag and viscous terms.

c. *A flat-bottomed Gulf of Mexico*

To examine the effect of the topography, we model the circulation in a domain shaped like the gulf in plan view but with a uniform depth of 1500 m. We use the same grid size and time step as in the previous case, leaving out the viscous terms and bottom drag.

The flow is significantly different in the absence of bottom topography as seen from Fig. 6. The circulation set up by the inflow does not occupy the entire basin. Instead of one clockwise cell, two counterrotating cells are formed in the basin. The shedding of eddies and their westward migration is much more regular and pronounced. We can clearly observe upwelling of cold saline water in the anticyclonic eddies, and downwelling of warm fresh water in cyclonic eddies.

Running the model in the same geometry without density variation reveals that the eddies in the above case are primarily due to baroclinic effects. Eddies

formed by the retroflected current intersecting itself in the barotropic case are much weaker.

d. *Comparison of numerical results with field observations*

Our numerical simulation of the gulf reproduces the observed anticyclonic circulation in the surface layers, the western boundary current, and the Loop Current that exhibits eddy shedding in the east. The most striking finding from the simulation is the strong cyclonic circulation in the lower layers along the steeply sloping shelf. This gyre is circulating in the opposite direction to the commonly seen anticyclonic flow in the upper layers. There is not much reference to this counterrotating gyre in the literature since most field studies are restricted to the upper layers of the ocean. The exception is a study by Hofmann and Worley (1986), who cite evidence for a deep cyclonic gyre in the western gulf and estimate its volume transport to be equal to that of the counterrotating gyre in the upper layers. Contour plots of the current velocity through sections across the gulf show the direction of the velocity being reversed at depths below 1000 m. Our numerical simulations support these findings and contradict Molinari et al. (1978) who claim that the deep water circulates in the same direction as in the upper layers.

The counter flowing current observed since the 1930s (cf. Hofmann and Worley 1986) inshore of the south flowing Florida Current and along the slope of the Florida shelf is visible in the numerical simulations where it forms a weak eddy at times. The observed clockwise return flow north of Cuba, the counterclockwise cell west of Florida, counterrotating eddy pairs in the central and western gulf, and the cyclonic circulation on the Campeche Bank north of the Yucatan are all reproduced in our numerical simulations. The flow on the Texas shelf observed by Nowlin and McLellan (1967), Molinari et al. (1978), and Hofmann and Worley (1986) is attributed to river inflows and does not show up in our simulation.

e. *Comparison with other numerical studies of the gulf circulation*

We compare our observations here with those of Hurlburt and Thompson (1980) and Dietrich and Lin (1994) who used a horizontal resolution of 20 km in their simulations of the gulf. We could afford a horizontal resolution of only 40 km on our workstation, but still resolved the main features. In addition, they integrated their solutions for 3–5 years, while our simulations have so far been carried out only for a period of 1–1.5 years.

Hurlburt and Thompson (1980) studied the dynamics of eddy shedding from the Loop Current using two-layer, barotropic and reduced gravity free-surface models in a rectangular domain with a grid spacing of approximately 20 km. A significant result of their study is that the eddy shedding occurs at its own natural period without any time variation in the inflow. This is in agreement with our own observations. They found that the eddy shedding is suppressed at low Reynolds numbers and reappears when the deep flow in the Yucatan is reduced. This suggests that topographic drag may play a role.

Dietrich and Lin (1994) modeled eddy shedding in the gulf using a primitive equation model on a Cartesian grid with coastline and bathymetry. They used 16 vertical levels and a 20-km resolution in the horizontal. They observed the western boundary current as part of the cyclonic circulation and also observed the deeper secondary anticyclonic circulation observed by us. Comparing this to Hurlburt and Thompson (1980), who use a rectangular domain, it becomes evident that the western boundary current and deep cyclonic circulation are observed only in models that take the shape of the ocean basin into account.

The cyclonic gyre produced in the absence of any wind stress in our simulations confirms that this large-scale feature is not primarily wind driven as was originally proposed by Sturges and Blaha (1976).

9. Conclusions

We have combined a number of algorithmic ideas to design an numerical solution procedure for the quasi-nonhydrostatic mesoscale ocean model. The procedure enables the implicit integration of the linear terms constituting the faster waves, while explicitly integrating the nonlinear terms constituting the slower waves. By treating the free-surface terms implicitly, we are able to choose a time step based on the fluid velocity rather than the free-surface gravity wave speed.

The numerical solution of our quasi-nonhydrostatic model with free surface is not much more expensive than the solution of the conventional hydrostatic equations even though a three-dimensional elliptic equation for pressure is solved at each stage in the time integration. This is because the directional inhomogeneity resulting from near-hydrostatic balance gives a special structure to the discretized elliptic equation. The solution of this equation is extremely fast when block relaxation is used within the multigrid algorithm. By using the free-surface formulation, we are thus able to trim the bulk of the additional computational cost involved with solving the elliptic equation in the nonhydrostatic model.

The model is implemented in general boundary-fitted curvilinear coordinates, has a moving top boundary and uses cell-centered variables. It satisfactorily simulates the flow in the Gulf of Mexico with its topographic variations. The results qualitatively compare with the numerical and field observations of other authors. Our numerical experiments reveal that the topography of the basin is largely responsible for the cir-

culation pattern being what it is. The free-surface elevation field developed due to the inflow and outflow and the shape of the basin are responsible for a clockwise circulation that follows the topographic contours. The direction induced by the topographic slope is, however, opposite to that induced by the free-surface tilt, and the direction of flow in the lower layers of the boundary current is anticlockwise and opposite in direction to that of the top layers. Intrusions of the Loop Current periodically pinch off to form eddies as they do in the gulf. The eddies migrate westward as Rossby waves. The model exhibits the baroclinic instability as well as upwelling and downwelling in clockwise and counterclockwise eddies.

Since the model is able to run for long periods without an eddy viscosity term in the horizontal momentum equations, we conclude that numerical viscosity, along with some filtering of the the vertical velocities, is sufficient to dissipate the subgrid-scale energy. Any further subgrid-scale parameterization may be included in the model, though it is questionable as to whether it is necessary.

The model performs smoothly when either the pressure or the normal velocity are specified at the outflow. When using these equations with the correct boundary conditions, it is unnecessary to use a sponge layer or enhanced viscosity at the inflow and outflow as is customary in primitive equation models.

The numerical solution of the equations is shown to be viable at a cost not much more than that of solving the hydrostatic equations.

By comparing solutions obtained with different values of the relaxation parameter β, we verify that the solution is not sensitive to a particular value of β, and that the relative error is indeed $O(\beta^{-1})$ as indicated by the scaling analysis.

10. Future work

The model developed could be used to study mesoscale processes and the effect of various factors on them. Additional factors such as wind stress and surface fluxes of heat and salt can easily be built into the model. The use of a stretched grid in the vertical would be appropriate to better resolve the density structure. Using realistic forcing, initial conditions and boundary data, we could make predictions of the flow field in the Gulf of Mexico or any other ocean. These could be compared to field observations as a means of evaluating the model.

What ocean modelers would most like to see is a comparison of the results from this model with those from one of the conventional hydrostatic models in use today. This sort of comparison would make sense only if both sets of model equations were solved in exactly the same numerical framework. This is difficult to achieve given that the hydrostatic model would need viscous terms, a buffer region outside the open boundaries, and different boundary conditions. Since we believe that this model is capable of predicting vertical velocities more accurately than the hydrostatic equations, we can use the computed vertical flux as a means of comparison. In an ongoing study that examines the role of mesoscale phenomena in vertically transporting nutrients for biological production, we are quantifying the amount of nutrient transported using this model, as well as from using the flow fields from the Semtner and Chervin (1992) model for comparison.

The model could be nested within a composite-adaptive grid framework to enable modeling more complex geometries, while locally resolving features in the flow when and where needed. It may be embedded in a global circulation model that would supply the boundary conditions for some region in which the mesoscale flow needs to be well resolved. This work was done while A.M. was at Stanford University.

Acknowledgments. This work was supported in part by the Institute of Naval Oceanography through a subcontract with the University Corporation for Atmospheric Research, and in part by ONR under Grant N00014-90-J-1344. We are grateful to Dr. Vincenzo Casulli for suggesting the numerical method for solving the free-surface problem and to Dr. Yan Zang for his guidance with the numerical solution of the incompressible equations.

REFERENCES

Boisvert, W. E., 1967: Major currents in the north and south Atlantic oceans between 64°N and 60°S. Tech. Rep., Naval Oceanographic Office, 92 pp.

Brandt, A., 1984: Multigrid techniques: 1984 Guide with applications to fluid dynamics. Lecture Notes, Computational Fluid Dynamics Lecture Series, von-Karman Institute for Fluid Dynamics, Belgium, 183 pp.

Casulli, V., 1995: Recent developments in semi-implicit numerical methods for free surface hydrodynamics *Advances in Hydroscience and Engineering,* Vol. II, Tsingua University Press, 2174–2181.

——, and R. T. Cheng, 1992: Semi-implicit finite difference methods for three dimensional shallow water flow. *Int. J. Numer. Methods Fluids,* **15,** 629–648.

——, and C. A. Lin, 1994: Numerical studies of eddy shedding in the Gulf of Mexico. *J. Geophys. Res.,* **99**(C4), 7599–7615.

Dukowicz, J. K., and R. D. Smith, 1994: Implicit free-surface for the Bryan–Cox–Semtner ocean model. *J. Geophys. Res.,* **99**(C4), 7991–8014.

Elliott, B. A., 1982: Anticyclonic rings in the Gulf of Mexico. *J. Phys. Oceanogr.,* **12,** 1292–1309.

Gill, A. E., 1982: *Atmosphere–Ocean Dynamics.* Academic Press, 662 pp.

Hofmann, E. E., and S. J. Worley, 1986: An investigation of the circulation of the Gulf of Mexico. *J. Geophys. Res.,* **91**(C12), 14 221–14 236.

Hurlburt, H. E., and J. D. Thompson, 1980: A numerical study of loop current intrusions and eddy shedding. *J. Phys. Oceanogr.,* **10,** 1611–1648.

Jones, H., and J. Marshall, 1993: Convection with rotation in a neutral ocean: A study of open-ocean deep convection. *J. Phys. Oceanogr.,* **23,** 1009–1039.

Kim, J., and P. Moin, 1985: Application of a fractional-step method to incompressible Navier–Stokes equations. *J. Comput. Phys.*, **59,** 308–323.

Leonard, B. P., 1979: A stable and accurate convective modeling procedure based on quadratic upstream interpolation. *Comput. Methods Appl. Mech. Eng.*, **19,** 59–98.

Levitus, S., 1982: *Climatological Atlas of the World Ocean.* NOAA Prof. Paper No. 13, U.S. Govt. Printing Office, 173 pp.

Lewis, J. K., and A. D. Kirwan, 1985: Some observations of ring topography and ring-ring interactions in the Gulf of Mexico. *J. Geophys. Res.*, **90**(C5), 9017–9028.

Mahadevan, A., 1995: A non-hydrostatic mesoscale ocean basin model with free-surface. Ph.D. thesis, Stanford University, 126 pp.

——, J. Oliger, and R. Street, 1996: A nonhydrostatic mesoscale ocean model. Part I: Well-posedness and scaling. *J. Phys. Oceanogr.*, **26,** 1868–1880.

Meakin, R. L., and R. L. Street, 1988: Simulation of environmental flow problems in geometrically complex domains. Part I: A general coordinate transformation. *Comput. Methods Appl. Mech. Eng.*, **68,** 151–175.

Molinari, R. L., J. F. Festa, and D. W. Behringer, 1978: The circulation of the Gulf of Mexico derived from estimated dynamic height fields. *J. Phys. Oceanogr.*, **8,** 987–996.

Nowlin, W. D., and H. J. McLellan, 1967: A characterization of the Gulf of Mexico waters. *J. Mar. Res.*, **25,** 29–59.

Pereyra, V., 1990: Geophysical Inversion Project, INTEGRA 3.2. Tech. Rep. 90-93, Weidlinger Associates, 34 pp.

Perng, C.-Y., 1990: Adaptive-multigrid computations for incompressible flows, including geometry, temperature and salinity effects. Ph.D. thesis, Stanford University, 257 pp.

Reid, R. O., 1972: A simple dynamic model of the loop current. *Contributions to the Physical Oceanography of the Gulf of Mexico,* L. R. A. Capurro and Joseph L. Reid, Eds., Vol. 2, Texas A&M University Oceanographic Studies, 157–159.

Semtner, A. J., Jr., and R. M. Chervin, 1992: Ocean general circulation from a global eddy-resolving model. *J. Geophys. Res.*, **97**(C4), 5493–5550.

Shapiro, R., 1970: Smoothing, filtering and boundary effects. *Reviews in Geophysics and Space Physics,* Vol. 8, Annual Reviews, 359–387.

Sturges, W., and J. P. Blaha, 1976: A western boundary current in the Gulf of Mexico. *Science,* **192,** 367–369.

Venkata, R., J. Oliger, and J. Ferziger, 1991: Composite grids for flow computations in complex 3D domains. *Proc. Fifth SIAM Conference on Domain Decomposition Methods for Partial Differential Equations,* SIAM, 426–431.

Vidal, V. M. V., F. V. Vidal, A. F. Hernandez, E. Meza, and J. M. Perez-Molero, 1994: Baroclinic flows, transports, and kinematic properties in a cyclonic-anticyclonic-cyclonic ring triad in a the Gulf of Mexico. *J. Geophys. Res.*, **99**(C4), 7571–7597.

Zang, Y., R. L. Street, and J. Koseff, 1994: A non-staggered grid fractional step method for time-dependent incompressible Navier–Stokes equations in general curvilinear coordinate systems. *J. Comput. Phys.*, **114,** 18–33.